PNAS RESEARCH ARTICLE | NEUROSCIENCE OPEN ACCESS

Functional specialization of hippocampal somatostatin-expressing interneurons

Simon Chamberland[a,b,1,2], Gariel Grant[a,b,1], Robert Machold[a,b], Erica R. Nebet[a,b], Guoling Tian[a,b], Joshua Stich[a,b], Monica Hanani[a,b], Klas Kullander[c], and Richard W. Tsien[a,d,2]

Contributed by Richard W. Tsien; received April 23, 2023; accepted February 27, 2024; reviewed by Lindsey L. Glickfeld, Jeffrey Magee, and Scott F. Owen

Hippocampal somatostatin-expressing (*Sst*) GABAergic interneurons (INs) exhibit considerable anatomical and functional heterogeneity. Recent single-cell transcriptome analyses have provided a comprehensive *Sst*-IN subpopulations census, a plausible molecular ground truth of neuronal identity whose links to specific functionality remain incomplete. Here, we designed an approach to identify and access subpopulations of *Sst*-INs based on transcriptomic features. Four mouse models based on single or combinatorial Cre- and Flp- expression differentiated functionally distinct subpopulations of CA1 hippocampal *Sst*-INs that largely tiled the morpho-functional parameter space of the *Sst*-INs superfamily. Notably, the *Sst;;Tac1* intersection revealed a population of bistratified INs that preferentially synapsed onto fast-spiking interneurons (FS-INs) and were sufficient to interrupt their firing. In contrast, the *Ndnf;;Nkx2-1* intersection identified a population of oriens lacunosum-moleculare INs that predominantly targeted CA1 pyramidal neurons, avoiding FS-INs. Overall, our results provide a framework to translate neuronal transcriptomic identity into discrete functional subtypes that capture the diverse specializations of hippocampal *Sst*-INs.

hippocampus | somatostatin interneurons | inhibition | disinhibition | circuits

Significance

GABAergic interneurons are important regulators of neuronal activity. Recent transcriptome analyses have provided a comprehensive classification of interneurons, but the connections between molecular identities and specific functions are not yet fully understood. Here, we identified and accessed subpopulations of interneurons based on features predicted by transcriptomic analysis. Functional investigation in transgenic animals revealed that hippocampal somatostatin-expressing interneurons (*Sst*-INs) can be divided into at least four subfamilies, each with distinct functions. Most importantly, the *Sst;;Tac1* intersection targeted a population of bistratified cells that overwhelmingly targeted fast-spiking interneurons. In contrast, the *Ndnf;;Nkx2-1* intersection revealed a population of oriens lacunosum-moleculare interneurons that selectively targeted CA1 pyramidal cells. Overall, this study reveals that genetically distinct subfamilies of *Sst*-INs form specialized circuits in the hippocampus.

A conserved feature of cortical circuits is the presence of numerous excitatory neurons whose activity is kept in check and coordinated by heterogeneous populations of GABAergic INs (1–4). IN heterogeneity is reflected in their neurochemical content, electrophysiological properties, anatomy, and connectivity (1, 2, 5). Because varied combinations of these features determine the specific function of each IN category, understanding how neuronal circuits process information requires a functional dissection of IN diversity. *Sst*-INs constitute a major fraction of INs in hippocampal area CA1 where they are largely found in stratum oriens and in the alveus (O/A) (1). As an integral part of the feedback inhibitory circuit, they control dendritic integration and pace network activity (6–8). While *Sst*-INs have been functionally studied as a single ensemble [(6, 9, 10) but see refs. 11 and 12], multiple studies provide clues to divisions in their neurochemical, anatomical, and electrophysiological properties (13–20). For example, the overall population of *Sst*-INs can target both principal neurons and FS-INs, resulting respectively in inhibition and disinhibition, two mostly opposing network effects (9, 21–24). Whether specific categories of *Sst*-INs account for these disparate circuit functions remains unknown.

Recent single-cell transcriptomic studies have provided deep insights into neuronal diversity at the molecular level. Transcriptomic heterogeneity is largely aligned with the traditional subdivision of neurons into superfamilies (25–27), including CA1 hippocampal *Sst*-INs, and indicates the existence of multiple subfamilies with distinct molecular profiles (3). While this transcriptomic classification approach allows for the identification of putative *Sst*-IN subpopulations, it inherently lacks the ability to directly predict or investigate functional specialization (3). Thus, a key challenge to understanding how molecularly defined *Sst*-IN subpopulations regulate brain circuitry is how to identify and experimentally access these neurons in situ.

Here, we describe a series of genetic approaches that leverages molecular profiling data to distinguish *Sst*-IN subtypes for experimental interrogation. We dissected the diversity of CA1 hippocampal *Sst*-INs by generating four lines of transgenic mice that were predicted to target distinct and minimally overlapping *Sst*-INs subpopulations. Our results revealed that the four subtypes of *Sst*-INs largely tile the anatomical and electrophysiological features attributed to *Sst*-INs overall, reducing the intrapopulation variation of most of the parameters sampled. We found that *Sst*-IN subtypes are highly specialized in the neurons they target, as exemplified by *Sst;;Tac1* bistratified INs that selectively target and interrupt FS-INs to disinhibit the CA1 microcircuit, in contrast to a subclass of

The authors declare no competing interest.

[1]S.C. and G.G. contributed equally to this work.

[2]To whom correspondence may be addressed. Email: simon.chamberland@nyulangone.org or richard.tsien@nyulangone.org.

This article contains supporting information online at https://www.pnas.org/lookup/suppl/doi:10.1073/pnas.2306382121/-/DCSupplemental.

Published April 19, 2024.

Ndnf;;Nkx2-1 OLM INs that preferentially innervate and inhibit CA1 pyramidal neurons (CA1-PYRs).

Results

A Genetic Dissection of *Sst*-IN Diversity. In the CA1 hippocampus, *Sst*-INs adopt multiple anatomical phenotypes defined by their axonal projections (13, 18). Whether anatomical differences can be aligned with genetically distinct neuronal subpopulations within the *Sst*-IN superfamily remains unclear.

To investigate the anatomical diversity of CA1 O/A *Sst*-INs, we bred *Sst*-Cre animals to the Ai9 reporter line and performed whole-cell recordings with biocytin fills from TdTomato+ INs in acute hippocampal slices (Fig. 1*A*). Post hoc anatomical tracings confirmed previous reports that hippocampal CA1 *Sst*-INs exhibit diverse axonal projection patterns (n = 25; Fig. 1*B* and *SI Appendix*, Fig. S1) (13, 14, 28). Anatomical heterogeneity of *Sst*-INs is paralleled at the transcriptomic level, and a large single-cell transcriptomic dataset containing CA1 *Sst*-INs is publicly available (3) (henceforth referred to as the Harris dataset). Transcriptomic datasets allow genetically similar neurons to be put closest to each other in principal component space, in turn represented on plots that render multidimensional information on 2D maps. We reasoned that genes or gene pairs that map onto restricted clusters of neurons and minimize intracluster distances would be good predictors of constituent subpopulations of neurons that might later prove to be functionally different. First, we used spatial dispersion statistics to uncover genes and pairs of genes, agnostic to gene identity, that minimized both the standard distance and the interquartile distance on the 2D map in the Harris dataset (Fig. 1*C* and *SI Appendix*, Figs. S2 and S3). Second, we mapped neurons expressing these genes and visually selected distinct populations (Fig. 1*D*). Consequently, we identified multiple combinations of genes that tiled the general population of *Sst*-INs (Fig. 1*D*) with minimal overlap at the individual cell level (Fig. 1*E*). To test the hypothesis that these genetic features identify functionally distinct *Sst*-IN subpopulations, we designed transgenic mice based on combinatorial expression of Cre- and Flp- recombinases (29). We therefore generated *Sst-Flp;;Tac1-Cre*, *Ndnf-Flp;;Nkx2-1-Cre,* and *Sst-Flp;;Nos1-CreER* transgenic lines (referred to as *Sst;;Tac1*, *Ndnf;;Nkx2-1* and *Sst;;Nos1*, respectively); we also leveraged the existing *Chrna2-Cre* line, motivated by the observation that *Chrna2* was one of the top ranked genes in our screening and prior knowledge that this transgenic line targets a specific subtype of *Sst*-IN (11).

We bred *Sst;;Tac1*, *Ndnf;;Nkx2-1*, *Sst;;Nos1*, and *Chrna2* mice to reporter lines (Ai65 for dual Cre-/Flp- recombinases and Ai9 for single Cre- recombinase), resulting in the expression of TdTomato in these neurons. Measuring the location of TdTomato+ somata as a function of distance from the pyramidal cell layer showed a cell type–specific distribution that largely recapitulated the general *Sst*-IN population (Fig. 1*F*). While *Sst;;Tac1*-INs were located closer to the CA1 pyramidal layer, *Ndnf;;Nkx2-1*-INs and *Chrna2*-INs were found progressively deeper in O/A; in contrast, *Sst;;Nos1*-INs were found mostly in the alveus, with some neurons sparsely distributed in strata radiatum and lacunosum-moleculare (LM) (Fig. 1*F*).

We next investigated the anatomy of neurons identified in transgenic lines with whole-cell recordings and biocytin fills, focusing on cells bodies within O/A, followed by post hoc anatomical reconstruction. In all cases, the axonal distribution revealed a preference for dendritic layers (Fig. 1*G* and *SI Appendix*, Figs. S4–S7 for all individual reconstructions), a feature typical of *Sst*-INs. Quantifying the axonal distribution across the CA1 layers revealed four distinct axonal projection patterns: 1) *Sst;;Tac1*-INs overwhelmingly targeted strata oriens and radiatum, a bilaminar morphology reminiscent of classically defined bistratified INs (2, 30); 2) *Ndnf;;Nkx2-1*-INs projected axons to both strata oriens and LM; 3) *Chrna2*-INs exhibited a strong and almost exclusive axonal projection to LM; and 4) *Sst;;Nos1*-INs mostly innervated stratum oriens (Fig. 1*H* and *SI Appendix*, Fig. S8 and Table S1). Finally, we associated the genetic identities of INs with commonly used anatomical categories based on the relative axonal distributions (see *Materials and Methods* for numerical criteria). The *Sst*-IN superfamily contained neurons from the OLM (n = 13), bistratified (n = 4), and oriens-oriens (n = 4) anatomical categories (Fig. 1 *I*, *Top*). We found that the OLMs were constituted by *Ndnf;;Nkx2-1*-INs (n = 10/13) and *Chrna2*-INs (n = 16/19), while the bistratified and oriens-oriens categories were disproportionately and almost exclusively represented by *Sst;;Tac1*-INs (n = 13/25) and *Sst;;Nos1*-INs (n = 12/15), respectively (Fig. 1 *I*, *Bottom*). Therefore, the wide-ranging anatomical features of *Sst*-IN categories can be largely accounted for by the morphologies of the genetically defined subtypes.

Electrophysiological Features of *Sst*-IN Subpopulations Explain the Observed Variation within the Superfamily. *Sst*-INs are generally known as regular-spiking INs and demonstrate a large hyperpolarization-activated cation current (I_h) (31). Variations in the firing patterns of *Sst*-INs have been reported before (17) and likely contribute to cell type–specific recruitment of these neurons during hippocampal activity (15, 30, 32), but whether the variation within the superfamily can be attributed to genetically defined cells remains unknown.

We next investigated the electrophysiological profiles of *Sst*-IN subtypes and compared them to the superfamily (Fig. 2*A*). While the firing frequency increased similarly with current injection across all *Sst*-INs subtypes (Fig. 2*B*), *Sst;;Nos1* demonstrated marked depolarization block (Fig. 2*B*). We next analyzed typical action potential (AP) parameters of the superfamily and subtypes and compared their intrapopulation variances (Fig. 2 *C–F* and *SI Appendix*, Fig. S9). Cell type-specific differences were evident (Fig. 2 *D–F* and *SI Appendix*, Fig. S9 and Table S2). For example, the AP maximal rate of fall was significantly different between most subpopulations (Fig. 2*D*; statistical treatment of complete dataset in *SI Appendix*, Table S2). In addition, the collective electrophysiological properties of these neurons largely accounted for the range of parameters found in the *Sst*-IN superfamily overall (Fig. 2 *D–F* and *SI Appendix*, Fig. S9). Furthermore, the coefficient of variation (CV) for these parameters was generally lower for all *Sst*-IN subpopulations (Fig. 2 *D–F* and *SI Appendix*, Fig. S9), compared to the superfamily (in 25 out of 32 cases). The tiling was sometimes incomplete (Fig. 2*E*), aligning with the fact that the four transgenic lines only partly cover the full transcriptomic space of the *Sst*-IN superfamily (Fig. 1 *D* and *E*). Overall, our recordings uncovered cell type–specific differences between *Sst*-IN subpopulations that help explain the variation of electrophysiological parameters within the superfamily.

We performed an unsupervised K-means cluster analysis to objectively assign the recorded neurons to groups and probe how much *Sst*-IN subpopulations could be distinguished on the basis of electrophysiological parameters alone (Fig. 2*G*). First, principal component analysis was performed on the eight electrophysiological parameters measured (*SI Appendix*, Table S3). K-means clustering using the first four principal components, which captured more than 90% of the variance, suggested the existence of two distinct clusters (elbow method). Cluster 1 incorporated almost all *Chrna2*-INs (26/27) and *Ndnf;;Nkx2-1*-INs (20/22). Cluster

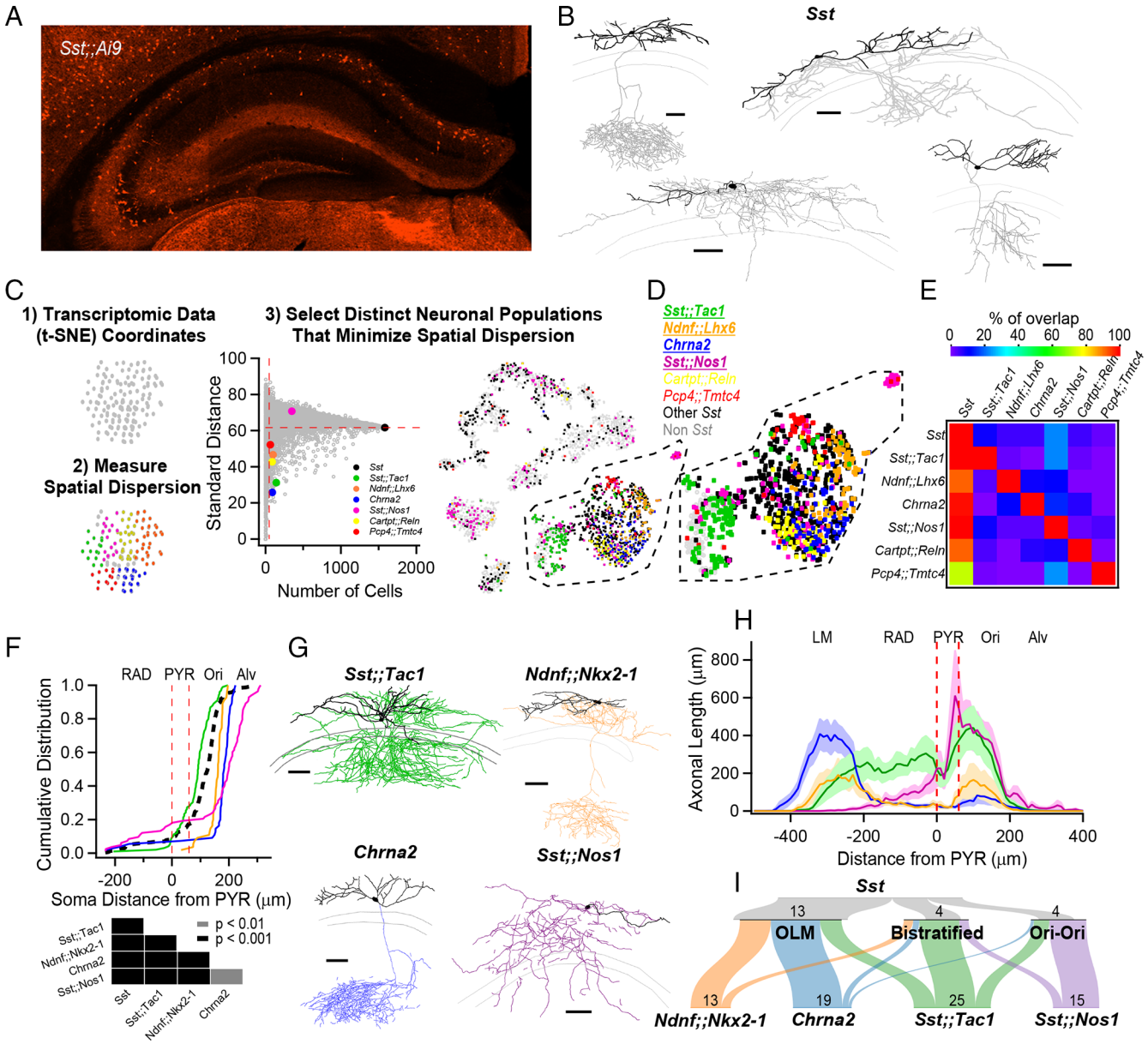

Fig. 1. Anatomical heterogeneity of hippocampal *Sst*-INs is partly solved by linking genetic identity to function. (*A*) Confocal image from an *Sst;;Ai9* mouse brain microsection showing the distribution of hippocampal neurons expressing the fluorescent protein TdTomato. In the CA1 region, *Sst*-INs are mostly found in stratum oriens/alveus (O/A). (*B*) Neurolucida reconstructions of CA1 O/A INs recorded in the *Sst;;Ai9* mouse model and filled with biocytin. Individual examples selected to highlight the diversity of axonal projections from these neurons (dendrites in black, axon in gray). Calibration bars = 100 μm. (*C*) Strategy to identify genes or pairs of genes delineating clusters of neurons that tile the larger *Sst*-IN population in the Harris et al. dataset (*Materials and Methods*). (*D*) Selection of gene pairs to generate intersectional transgenic mouse models (bold and underlined), and pairs of genes which could potentially label specific subpopulations for which mice were not generated. The gene *Chrna2* by itself fulfills the established criteria and enabled the use of a pre-existing transgenic mouse line (11). All residual cells expressing a nonzero level of *Sst* transcripts are shown in black, and all other cells are shown in light gray. (*E*) Matrix showing little overlap of subsets of neurons expressing the selected combination of genes. Two potential gene pairs additionally identified within the Harris dataset are shown. Percentage of overlap color coded, where red represents 100% overlap and violet represents 0% overlap. Percentages normalized relative to diagonal (100%). (*F*) Quantification of the localization of fluorescently labeled cell bodies in the five genotypes relative to the PYR layer in the CA1 hippocampus. Table below reports the *P*-values from KS tests between the five genotypes after Holm–Bonferroni correction for multiple comparisons. (*G*) Neurolucida reconstructions of representative interneurons visually targeted for recording by the expression of a fluorescent reporter in the different transgenic mouse models. Individual neurons were recorded and filled with biocytin (axons colored according to genotype, dendrites in black). Calibration bars, 100 μm. (*H*) Histogram of axonal distribution for all interneurons recorded and filled in the four transgenic mouse models as a function of distance from the pyramidal cell layer (indicated by the dashed red lines). The shaded areas correspond to the SE. (*I*) Sankey diagrams showing the segregation of *Sst*-INs into three broadly defined anatomical categories, OLM, bistratified and oriens-oriens (*Top*); the genetically identified subclasses (*Bottom*) capture and tile the three general anatomical categories of *Sst*-INs, and further refine the within-genotype anatomical identity. Number of reconstructed neurons is shown.

2 captured all the *Sst;;Nos1*-INs (8/8) and most, but not all *Sst;;Tac1* -INs (25/32), overall, far from a random distribution ($P < 0.0001$ by χ^2 test). Thus, unsupervised K-means cluster analysis indicated that our genetically based sorting of *Sst*-IN subpopulations aligned in large part with segregation solely based on electrophysiological properties.

Cell Type–Specific Targeting by Subpopulations of *Sst*-INs. We and others have previously shown that the superfamily of *Sst*-INs targets both CA1-PYRs and FS-INs in the CA1 region (9, 21). In our recent study (21), a small dataset of paired-recordings suggested that *Sst*-expressing bistratified but not OLM cells targeted FS-INs, hinting at cell type–specific connectivity. It remains unknown

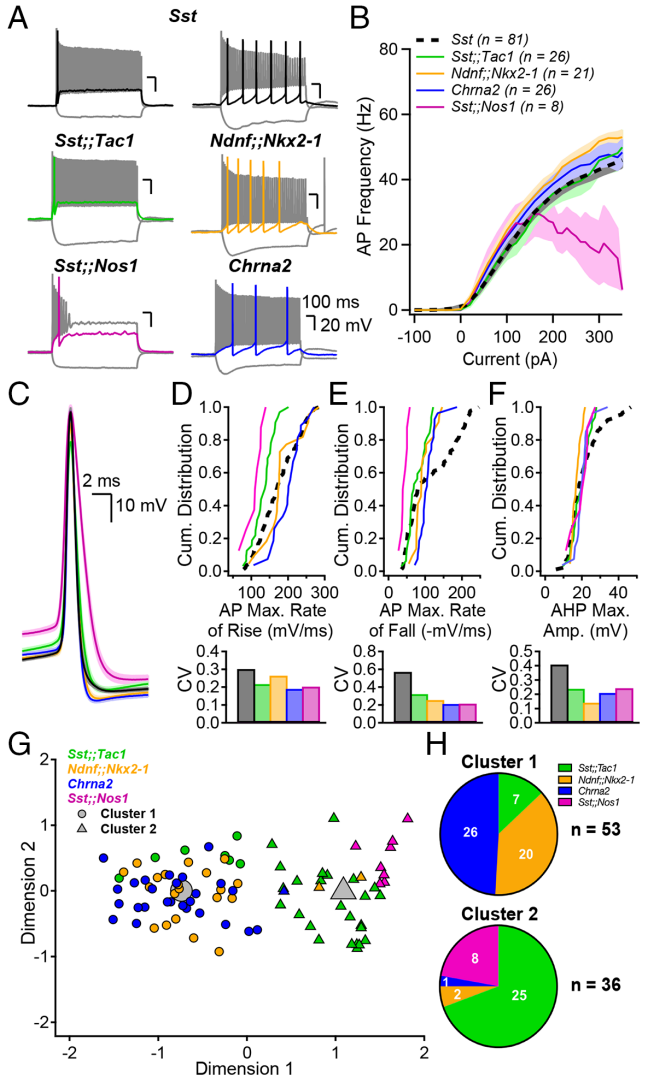

Fig. 2. Genetically defined subpopulations of *Sst*-INs tile the electrophysiological parameter space and account for the heterogeneity within the *Sst* family. (*A*) Membrane potential changes resulting from hyperpolarizing and depolarizing current pulses in the five transgenic mouse models indicated. Each panel includes a response to hyperpolarizing pulse driving V_m between −100 and −90 mV, a response to rheobase current pulse (color), and the maximal firing rate response (gray). (*B*) Firing frequency as a function of current injection amplitude. Number of averaged cells is shown. (*C*) Action potential waveforms elicited by rheobase current, aligned at peak overshoot, averaged across all interneurons in each subgroup. Shaded areas correspond to SE. (*D*) *Top*, Cumulative distribution of the AP maximal rate of rise (mV/ms) for the five genotypes and associated coefficients of variation (CV, *Bottom*). (*E* and *F*) Same as (*D*) but for the AP maximal rate of fall (*E*) and the AP afterhyperpolarization maximal amplitude (*F*). (*G*) Principal component analysis followed by unsupervised K-means clustering analysis using the electrophysiological parameters above and in *SI Appendix*, Fig. S9 divides the neurons into two clusters. (*H*) Pie charts summarizing the distribution of the genetically identified interneuron subgroups across electrophysiologically defined clusters. The distribution of neurons was significantly different than expected by chance (Chi-square = 54.751, $P < 0.0001$).

whether *Sst*-IN subtypes generally provide nonselective or cell type–specific inhibition to their targets.

Optogenetic circuit mapping revealed clear target preference among *Sst*-IN subfamilies (Fig. 3). Postsynaptic targets were visually identified and electrophysiologically confirmed as CA1 pyramidal cells (CA1-PYRs), FS-INs, and RS-INs with a hyperpolarizing sag (putative *Sst*-INs) before performing voltage-clamp recordings at 0 mV. Optogenetic stimulation (20 ms pulse) of presynaptic *Sst;;Tac1*-INs revealed large amplitude inhibitory postsynaptic currents (IPSCs) in FS-INs (116.1 ± 27.7 pA, n = 20); yet, with the same photostimulation, significantly smaller IPSCs in CA1-PYRs (20.8 ± 6.4 pA; n = 12; $P < 0.001$, Mann–Whitney *U* test) and RS-INs (12.2 ± 2.8 pA; n = 24; $P < 0.001$, Mann–Whitney *U* test; Fig. 3 *A* and *B*). In sharp contrast, photostimulation of *Ndnf;;Nkx2-1*-INs generated significantly larger IPSCs in CA1-PYRs (21.7 ± 2.8 pA; n = 14) than in FS-INs (10.2 ± 2.3 pA; n = 9; $P < 0.01$, Student's *t* test) or RS-INs (1.6 ± 0.9 pA; n = 5; $P < 0.001$, Mann–Whitney *U* test; Fig. 3 *A* and *B*). On the other hand, optogenetic stimulation of *Chrna2*-INs resulted in similar IPSCs in CA1-PYRs (25 ± 5.6 pA; n = 10) and FS-INs (21.6 ± 3.9 pA; n = 12; $P > 0.4$, Mann–Whitney *U* test), that were both much larger than the IPSCs recorded in RS-INs (0.9 ± 0.7 pA; n = 3; $P < 0.05$ vs. CA1-PYRs and $P < 0.01$ vs. FS-INs, Mann–Whitney *U* test). Finally, photostimulation of *Sst;;Nos1*-INs revealed almost undetectable IPSCs in the three targets (CA1-PYRs: 0.6 ± 0.5 pA; n = 4; FS-INs: 0.5 ± 0.4 pA, n = 15; RS-INs: 0 pA, n = 9) despite obvious axonal arborization in O/A. Similar results were obtained when circuit mapping was performed with intracellular Cs^+-based solution to improve voltage-clamp (*SI Appendix*, Fig. S10 and associated legend). To ask how well the subtypes accounted for the impact of *Sst*-positive neurons as a whole, we calculated the sum of IPSC amplitudes evoked by *Sst;;Tac1*-INs, *Ndnf;;Nkx2-1*-INs, *Chrna2*-INs, and *Sst;;Nos1*-INs (Fig. 3*B*, red dotted lines labeled ∑). The summed subgroup events represented 85% of the IPSC in CA1-PYRs directly recorded upon by optogenetic stimulation of the general *Sst*-IN population; for FS-INs, the corresponding percentage was 75%. This suggests that our strategy captured the bulk of *Sst*-INs innervating CA1-PYRs and FS-INs. Moreover, the four *Sst*-IN subtypes hardly influenced regular-spiking INs with a hyperpolarizing sag (Fig. 3 *A* and *B*), consistent with the notion that *Sst*-INs mostly avoid synapsing with each other (33).

For a direct comparison of the relative preference for FS-INs and PYRs, we performed sequential recordings of IPSCs from neighboring CA1-PYRs and FS-INs in response to identical optogenetic stimulation. We analyzed the synaptic strength in these pairs by determining the ratio $[IPSC_{FS\text{-}IN}/(IPSC_{FS\text{-}IN} + IPSC_{PYR})]$ as an index of FS-IN preference, 0.5 indicating no preference. This normalization circumvented potential confounds including different transgenic animal models, number of presynaptic axons in the slice and optrode placement (Fig. 3*C*). These experiments confirmed a strong preference of *Sst;;Tac1*-INs for FS-INs over CA1-PYRs (ratio of 0.91 ± 0.03; n = 7 pairs). In contrast, *Ndnf;;Nkx2-1*-INs were found to preferentially target CA1-PYRs (ratio of 0.26 ± 0.04; n = 9 pairs; $P < 0.0001$, unpaired *t* test; Fig. 3 *C* and *D*). Similar results were obtained with Cs^+ intracellular solution, confirming the target specificity of *Sst;;Tac1*-INs and *Ndnf;;Nkx2-1*-INs (*Sst;;Tac1* ratio 0.78 ± 0.03, n = 13; *Ndnf;;Nkx2-1* ratio 0.17 ± 0.04, n = 12, $P < 0.0001$, Mann–Whitney *U* test). Finally, *Chrna2*-INs contacted both FS-INs and CA1 pyramidal cells without clear preference (K^+ intracellular: ratio of 0.50 ± 0.07; n = 9; Cs^+ intracellular: ratio of 0.33 ± 0.11; n = 9; Fig. 3 *C* and *D*). For recordings performed with Cs^+ intracellular, the ratio exhibited a slight shift toward CA1-PYRs for all genotypes, a finding consistent with a more distal location of synapses on CA1-PYRs compared to FS-INs. This also suggests that the ratio is an approximation subject to the usual limitations of voltage-clamp but allows for comparison between genotypes in a given condition. These results, obtained with fixed optogenetic stimulation, provide strong evidence that *Sst*-IN subpopulations vary widely in their targeting of other neuron types and are thus functionally specialized.

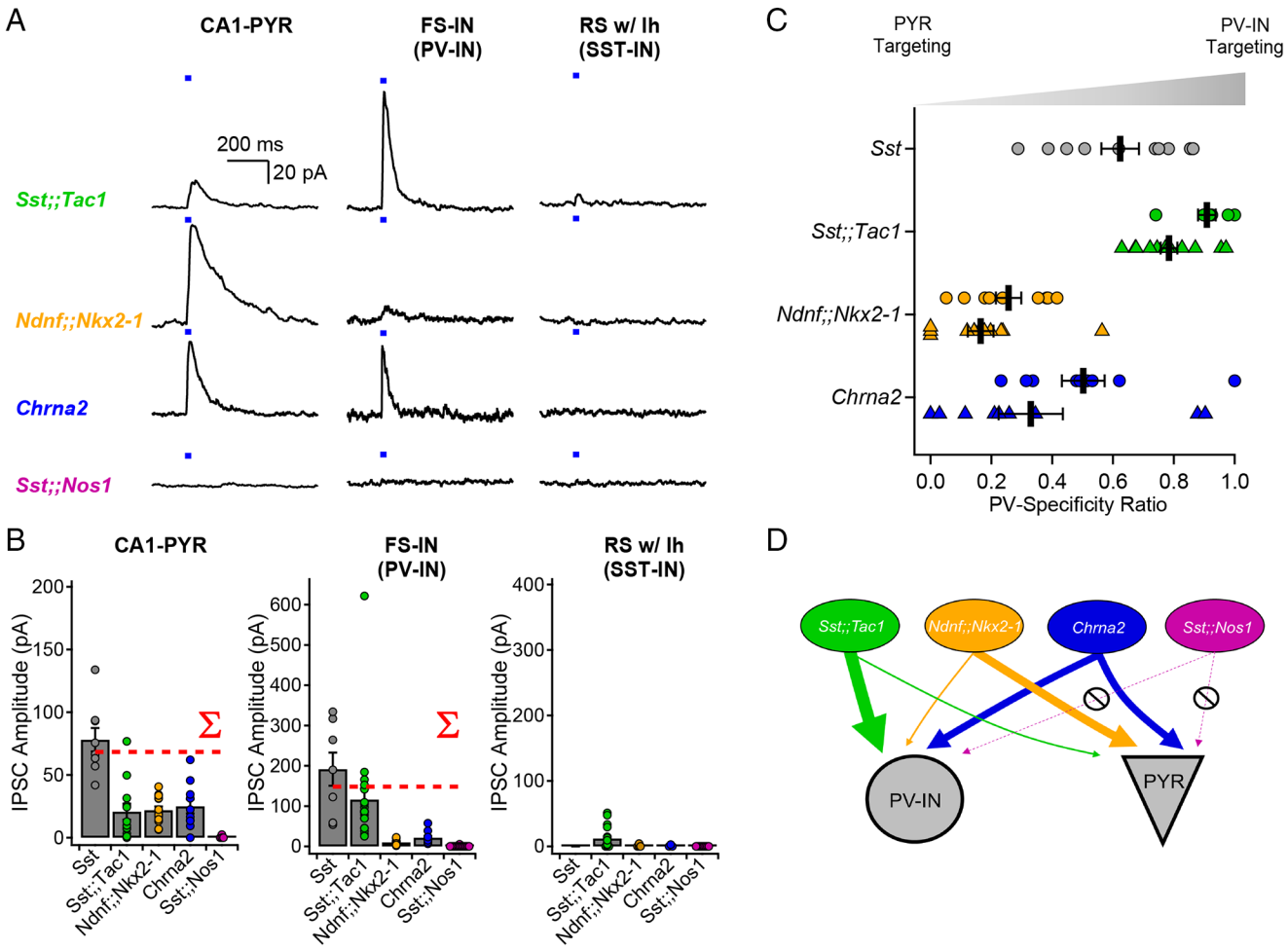

Fig. 3. Optogenetic circuit mapping reveals that postsynaptic targets of *Sst*-INs are subpopulation-specific. (*A*) Voltage-clamp recordings (holding potential = 0 mV) from pyramidal cells, fast-spiking interneurons, and regular-spiking interneurons with prominent sag, showing representative IPSCs generated by optogenetic activation of IN subpopulations. (*B*) Summary bar graph of IPSC amplitudes recorded in the three target types. The dotted red lines show the arithmetic sums of IPSCs generated by photostimulation of the individual subpopulations. Data for *Sst*-INs photostimulation recorded in FS-INs partly replotted from Chamberland et al. (21) (Fig. 2*J*). (*C*) Sequential recordings from neighboring fast-spiking interneurons and pyramidal cells reveals target-specificity of *Sst;;Tac1*-INs, *Ndnf;;Nkx2-1*-INs, and *Chrna2*-INs. Circles show sequential recordings performed with K^+ internal solution and triangles show sequential recording performed with Cs^+ internal solution. (*D*) Cartoon depicting the target selectivity of *Sst*-IN subpopulations. Average ± SEM is shown.

***Sst;;Tac1*-INs Are Sufficient to Interrupt FS-INs.** We now turn to the use of subgroup-specific mouse lines as experimental tools. We recently reported that FS-INs undergo a strikingly persistent interruption of firing upon brief synaptic inhibition, resulting in CA1-PYR disinhibition (21). The interruption of firing was induced by optogenetic stimulation of the general *Sst*-INs population, but whether this function is exclusive or shared among multiple *Sst*-IN subpopulations remains unclear.

FS-INs were depolarized to trigger their characteristic fast-spiking and nonadapting firing patterns, and presynaptic subpopulations of *Sst*-INs were optogenetically stimulated. We found that photostimulation of subgroups failed to induce the interruption of firing in the case of *Ndnf;;Nkx2-1*-INs (0% likelihood, n = 5), *Chrna2*-INs (0.9 ± 0.8% likelihood, n = 11), and *Sst;;Nos1*-INs (0% likelihood, n = 4) (Fig. 4 *A*–*C*). In contrast, *Sst;;Tac1*-INs reliably generated the interruption of firing (77 ± 7% likelihood, n = 15; Fig. 4 *A*–*C*) even with only one light pulse. *Sst;;Tac1*-INs triggered the interruption of firing with similar likelihood and dynamics (Fig. 4 *B* and *C*) as the general *Sst*-INs population (86.1% ± 2.4%, n = 29, $P > 0.1$) (*Sst* data previously reported in ref. 18). Thus, we conclude that among the *Sst*-IN subgroups, the *Sst;;Tac1*-IN subgroup was quantitatively sufficient (Fig. 4 *A*–*C*) to reliably trigger the persistent interruption of firing. Therefore, these results establish *Sst;;Tac1*-INs in the CA1 hippocampus as a functionally distinctive subclass of disinhibitory INs, equipped with exceptional potency to relieve pyramidal neurons from feedforward inhibition (21).

Diverse Dynamics of *Sst*-IN Subtype Recruitment during Hippocampal Activity. INs exhibit cell type–specific responses to synaptic inputs from the same origin (34, 35). For example, excitatory synapses onto *Sst*-INs generally demonstrate short-term facilitation (34, 36), whereas short-term depression is typically observed in neighboring *Pv*-INs (37). In addition, the cell type–specific dendritic arbors uncovered here could contribute to the selective integration of synaptic inputs (*SI Appendix*, Fig. S8). We next investigated how repetitive stimulation of hippocampal CA3 axons recruits *Sst*-IN subtypes.

We initially compared the recruitment profile of hippocampal CA1 *Sst*-INs with that of *Pv*-INs (Fig. 5*A* and *SI Appendix*, Fig. S12 *A* and *F*), respectively, operating as feedback (*SI Appendix*, Fig. S1) and feedforward (*SI Appendix*, Fig. S11) elements. Schaffer collaterals (SC) were stimulated 5 times at 50 Hz, a protocol shown to discriminate between late-persistent and early-onset INs (7). Our results (Fig. 5 *A* and *B*) confirmed the notion that most *Sst*-INs are late-persistent and *Pv*-INs are generally onset-transient INs (2, 7), with individual neurons from these superfamilies sometimes demonstrating intermediate features (*SI Appendix*, Fig. S12 *A* and *F*). Next, we characterized the recruitment of *Sst*-IN

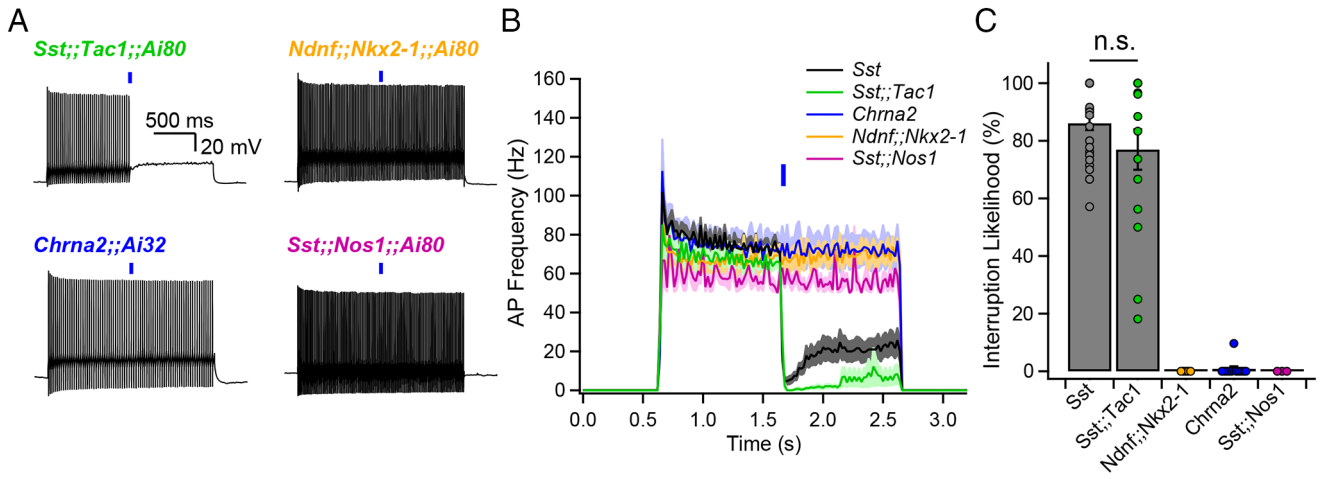

Fig. 4. *Sst;;Tac1*-INs are sufficient to interrupt fast-spiking interneurons. (*A*) Representative examples showing optogenetic activation of *Sst*-IN subpopulations during sustained fast-spiking interneuron firing evoked by steady current. (*B*) Bar graph showing the average firing as a function of time before and after optogenetic stimulation of *Sst* subpopulations. (*C*) Summary bar graph indicating that *Sst;;Tac1*-INs are sufficient within the general *Sst*-IN population to interrupt fast-spiking interneurons. Average ± SEM is shown.

subtypes. We found that *Sst;;Tac1*-INs were recruited early and maintained their firing during repetitive SC stimulation (Fig. 5*C* and *SI Appendix*, Fig. S12*B*). In contrast, *Ndnf;;Nkx2-1*-INs and *Chrna2*-INs were late-persistent (Fig. 5*C* and *SI Appendix*, Fig. S12 *C* and *D*), with some neurons showing nonmonotonic recruitment, more likely so for *Ndnf;;Nkx2-1*-INs. Finally, *Sst;;Nos1*-INs exhibited onset-transient recruitment (Fig. 5*C* and *SI Appendix*, Fig. S12*E*).

The different patterns of recruitment of INs arose from a combination of 1) circuit; 2) synaptic; and 3) intrinsic properties as studied by systematic current clamp and voltage clamp experiments (*SI Appendix*, Figs. S12–S14). First, the EPSP and AP latencies generated by individual SC stimuli (Fig. 5 *D* and *E*) confirmed that *Pv*-INs were overwhelmingly recruited by CA3 inputs, while *Sst*-INs were predominantly recruited by the disynaptic CA3-CA1 loop (Fig. 5 *D* and *E* and *SI Appendix*, Fig. S13 *A–C*). *Sst;;Tac1*-INs demonstrated intermediate EPSP and AP latencies, while *Ndnf;;Nkx2-1*-INs, *Chrna2*-INs, and *Sst;;Nos1*-INs were all recruited later in time, indicative of innervation by CA1-PYRs (Fig. 5 *D* and *E* and *SI Appendix*, Fig. S13 *A–C*). We further observed that EPSPs evoked by a single stimulation could have two peaks separated by ~5 ms, consistent with the idea that some INs are innervated by both CA3- and CA1-PYRs. This was most often seen in *Pv*-INs and *Sst;;Tac1*-INs, rarely in the general *Sst*-IN superfamily and in *Sst;;Nos1*-INs, and never in *Ndnf;;Nkx2-1*-INs and *Chrna2*-INs (*SI Appendix*, Fig. S13 *A–C*). Second, the short-term dynamics of EPSP amplitudes during trains further supported this notion (Fig. 5 *D* and *E* and *SI Appendix*, Fig. S13 *A–C*). In *Sst;;Tac1*-INs, the CA3 EPSP displayed stable amplitudes during trains, while the CA1 EPSP showed short-term facilitation (*SI Appendix*, Fig. S13 *A–C*). This observation was validated in voltage-clamp recordings (*SI Appendix*, Fig. S14) wherein the distinction between CA3 (feedforward) and CA1 (feedback) inputs to *Sst;;Tac1*-INs was most clear (*SI Appendix*, Fig. S14*A*1). On the other hand, *Ndnf;;Nkx2-1*-INs and *Chrna2*-INs both demonstrated extensive short-term facilitation (*SI Appendix*, Figs. S13 *A–C* and S14). Third, we asked why *Sst;;Tac1*-INs recruitment was still somewhat limited despite dual CA3 and CA1 innervation, as APs could theoretically be evoked on individual or summated EPSPs from CA3 and CA1 inputs. While the input resistance of *Sst;;Tac1*-INs was consistent with other subpopulations, we found that their membrane time constant was faster than most other *Sst* subtypes (*SI Appendix*, Fig. S13 *D* and *E*; see Legend for statistical reporting), thus limiting synaptic integration. Overall, we dissected the circuit, synaptic and cell intrinsic factors contributing to the differential recruitment of *Sst*-IN subtypes. We further identified *Sst;;Tac1*-INs as a population of cells atypically recruited by both CA3 and CA1 excitatory afferents, that respond to CA3 input by generally firing after *Pv*-INs but before most other *Sst*-INs.

Discussion

Vast heterogeneity among hippocampal INs has been described based on anatomical, neurochemical, electrophysiological, and functional criteria (1, 2, 38). Using single-cell transcriptomic data, which provided a likely complete survey of these cells (3), we performed spatial dispersion analysis to predict genetic features identifying minimally overlapping *Sst*-IN subpopulations. To test the hypothesis that these genetic features provide labels to access functionally distinct *Sst*-IN subpopulations, we generated and leveraged transgenic animals. The mouse lines we assembled largely recapitulate the overall synaptic weight and broad spectrum of features of *Sst*-INs as a whole. The four tagged subpopulations are distinguishable by a combination of cell-autonomous features, output connectivity, input responsivity, and functional impact (Fig. 6). In brief, the *Sst;;Tac1* line labeled morphologically bistratified INs, providing the first genetically driven access to a population of bistratified neurons. The *Sst;;Nos1* line tagged INs with somata closest to the alveus and diffuse axonal trees, easily distinguishable from other *Sst*-INs. Two other subtypes shared OLM morphology but were readily distinguished based on their target specificity: *Ndnf;;Nkx2*-1-INs preferentially targeted PYRs over FS-INs, while *Chrna2*-INs (11) lacked PYR vs. FS-IN preference.

Sst;;Tac1-INs preferentially targeted FS *Pv*-INs. This suggests that *Sst;;Tac1*-INs may represent a subgroup of anatomically identified bistratified cells, given previous reports showing that bistratified cells densely innervate CA1-PYRs dendritic trees (13, 30, 39–42). Thus, *Sst;;Tac1*-INs are particularly well-suited for disinhibition of CA1-PYRs (21), analogous to subpopulations of *Vip*-INs (43–46). These two types of INs might play complementary circuit roles: *Sst;;Tac1*-INs prefer FS *Pv*-INs over RS *Sst*-INs (Fig. 3 *C* and *D*), opposite to disinhibitory *Vip*-INs, which preferentially innervate RS *Sst*-INs over FS *Pv*-INs (21). These disinhibitory circuits could be crucial to control IN activity during hippocampal activity. PV-INs and SST-INs are active at different phases of theta oscillations, and PV-INs are strongly active

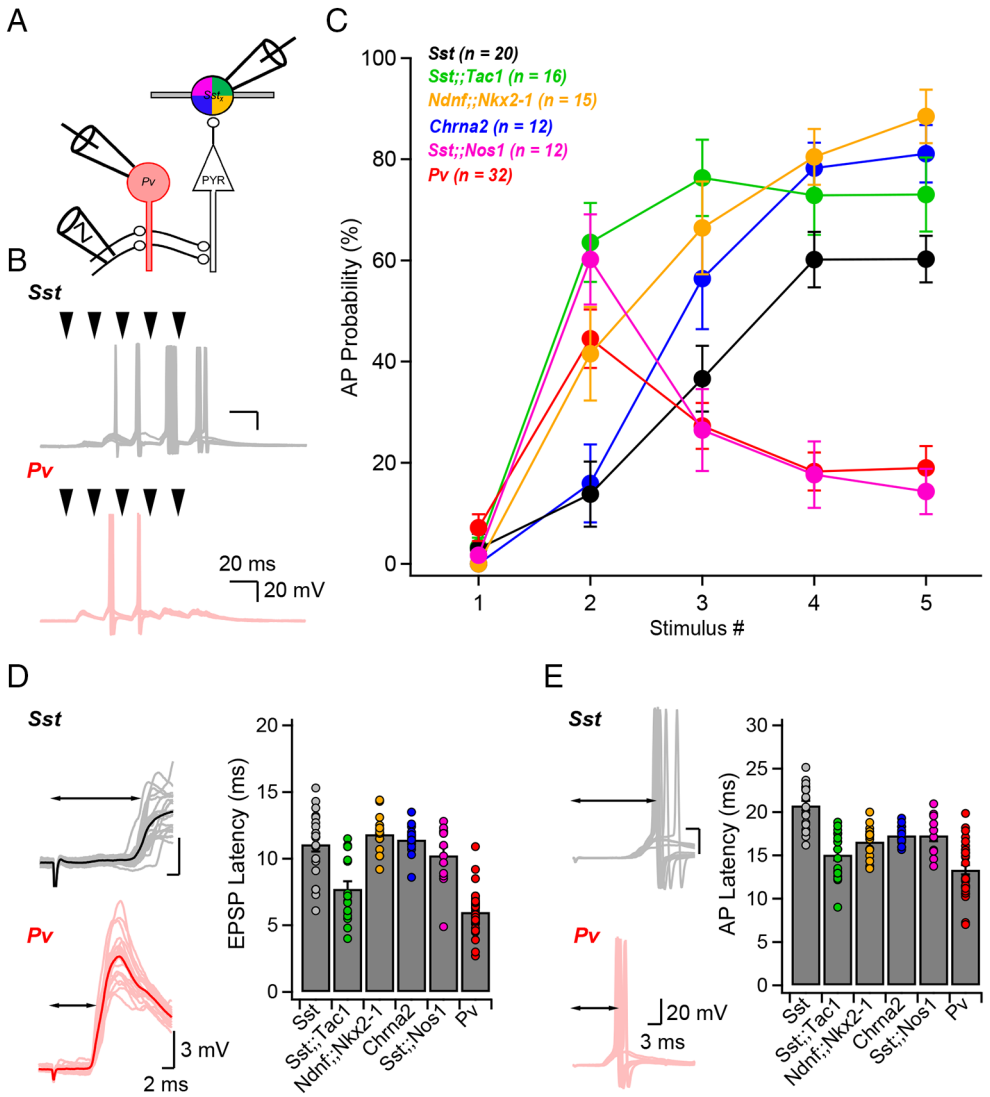

Fig. 5. Differential recruitment of *Sst*-IN subtypes during hippocampal CA3 activity. (*A*) Schematic of the recording configuration. (*B*) Schaffer collaterals stimulation (5 pulses delivered at 50 Hz) results in late-persistent recruitment of *Sst*-INs and early-onset recruitment of *Pv*-INs. (*C*) Action potential probability as a function of stimulus number for the interneurons recorded. Traces show average ± SEM. (*D* and *E*) EPSP latency (*D*) and action potential latency (*E*) measured for interneurons in the six genotypes investigated. Bar graphs show average ± SEM. Number of cells reported correspond to that reported in panel (*C*).

during sharp wave ripples while SST-INs are mostly silenced (5). Differential recruitment of INs through inhibitory control in the hippocampus would be reminiscent of cortical *Vip*-INs, which selectively silence specific categories of *Sst*-INs during whisking (47). Having intersectional mouse lines readily available for optogenetic or pharmacogenetic manipulation will hasten future testing of such circuit predictions and their behavioral implications.

Dynamic recruitment of INs by repetitive inputs as reported here likely joins specific connectivity to enable cell type–specific recruitment during different hippocampal rhythms. Short-term facilitation has long been recognized at excitatory synapses formed by CA1-PYRs onto *Sst*-INs (34, 36), partly owing to the expression of the extracellular leucine-rich repeat fibronectin containing 1 protein (*Elfn1*) acting transsynaptically to control glutamate release (35, 48). Our results further highlight that the heterogeneous profiles of short-term facilitation previously identified in the *Sst*-IN superfamily can be mostly associated with different genetically identified subtypes (34, 49). The different short-term dynamics of release could be supported by the variable expression of *Elfn1* across the 4 subtypes of *Sst*-INs studied. Transcriptomics data suggest the weakest *Elfn1* expression in *Sst;;Tac1*-INs and *Sst;;Nos1*-INs (3), an observation consistent with the limited facilitation in these cells. However, this explanation is unlikely to fully explain the phenotypes observed—our finding that the CA3 and CA1 inputs received by *Sst;;Tac1*-INs exhibit different release dynamics suggest that additional mechanisms will need to be considered.

Together, the *Ndnf;;Nkx2-1*-OLMs and *Chrna2*-OLMs divide the OLM category into two functionally distinct populations (Fig. 6). Taking advantage of large numbers of genetically marked cells, we found significant differences in somatic location (Fig. 1*F*), axonal apportionment (Fig. 1*G*), electrophysiological properties (Fig. 2), target specificity (Fig. 3), and recruitment dynamics (Fig. 5). It is interesting to compare these findings with studies that start with morphofunctionally identified OLM INs (50) or that emphasize developmental origin or expression of ionotropic 5HT3aR serotonin receptors (16). Knowing the genetic profile of *Ndnf;;Nkx2-1*-OLMs and *Chrna2*-OLMs (3) provides a potential starting point but neither of these subpopulations show a pattern of 5HT3aR transcript expression or transcripts consistent with caudal ganglionic eminence origination. Examination of other tiles in the emerging mosaic of *Sst*-INs (Fig. 1), particularly for additional OLM subtypes, would be a logical next step before drawing firm conclusions. This is partly motivated by our transcriptomic analysis

suggesting that we are likely missing three additional *Sst*-IN subtypes. These subpopulations might be responsible for electrophysiological features still unaccounted for in the *Sst*-IN superpopulation (Fig. 2 and *SI Appendix*, Fig. S9) and rarer anatomical categories such as septo-hippocampal or backprojecting cells that we did not encounter but that are known to exist (5). Large-scale efforts in the cortex have shown that morpho-electrophysiological and transcriptomics (MET) parameters converge to describe interneuronal categories (51–53), with the advantage that each cell is individually sampled for MET features. This would be an alternative starting point in designing intersectional transgenic animals that target missing or less frequently encountered hippocampal interneuron subpopulations to probe their circuit function.

Our findings show practical outcomes of a strategy that leverages single-cell transcriptomics (3), classical morpho-physiological analysis (1, 2, 5), and functional input/output connectivity of neuronal subgroups (workflow in first row of Fig. 6). There was no a priori guarantee that tiling based on genetic markers would generate subgroups set apart by morpho-physiological distinctions, as our experiments ultimately demonstrated. We suspect that the success of this strategy was not fortuitous—marker genes may reflect deeper differences in gene expression, extending to mechanistically important genes for ion channels, adhesion proteins and developmentally critical transcription factors, etc. (54, 55). A fully bottom–up approach might seem less chancy, but knowledge of genotype–phenotype relationships is still too primitive to support this route. Meanwhile, there may be merit in the pragmatic strategy of using transcriptomic data to predict genetic features identifying distinct and minimally overlapping *Sst*-IN subpopulations, then taking the risk of generating intersectional transgenic animals. Transgenic mouse lines expressing recombinases under specific promoters have limitations as experimental models, including off-target transgene expression which could originate from either bonafide expression of the gene in undesirable cells or Cre- leakage. This is true for several mouse lines including the *Sst*-Cre line which clearly labels a population of CA3 pyramidal cells when bred with reporter lines, an observation adding motivation for this study. The intersectional strategy employed here logically decreased the likelihood of observing off-target expression as two recombinases are required in a given cell to allow transgene expression, and indeed, we observed no marker expression in pyramidal cells in our intersectional lines. In the *Chrna2*-Cre mouse model (11), the great majority of labeled cells are INs, while only a small proportion (conservative upper bound, ~4%) have anatomical features consistent with pyramidal cells (11). The transgenic lines are themselves an end product amenable to functional analysis, both by classic single-cell approaches, and by optogenetics on pooled subgroups to determine output connectivity and functional impact (Figs. 3 and 4). Like any iterative process of divide and conquer (e.g. Twenty Questions or expression cloning), the assignment of functional roles to even narrower subgroups might be achieved via multiple paths even when the final result is unique. Having a functional assay (e.g., Fig. 4) provides empirical guidance for the winnowing down procedure and discourages oversplitting (56).

The study of interneuronal function has been greatly accelerated by the development of transgenic animals coupled with optogenetics (57–61), enabling in situ identification and selective manipulation of sparse neuronal types (2, 26, 62). Our findings demonstrate that the transcriptomic profiles of neurons have predictive value for accessing and characterizing subpopulations of neurons, gained via transgenic animals or potentially other approaches (63–66). The tiling strategy developed here to dissect *Sst*-INs could be extended to other groups of neurons, in other brain regions. Genetic access to functionally unified groups of neurons will expedite dissection of circuit function and clarify overriding relationships between neuronal structure and function (11, 12, 67, 68).

Materials and Methods

Animals and Breeding Strategies. All experiments performed here were approved by the Institutional Animal Care and Use Committee (IACUC) at New York University Langone Medical Center. The experiments reported in this paper involved the use of 12 transgenic mouse lines. *Sst;;Tac1* animals were obtained by crossing *Sst*-Flp [Sst$^{tm3.1(flpo)Zjh}$/AreckJ, JAX stock #28579, (29)] with *Tac1*-Cre [B6;129S-Tac1$^{tm1.1(cre)Hze}$/J, JAX #021877, (69)] mice, and were

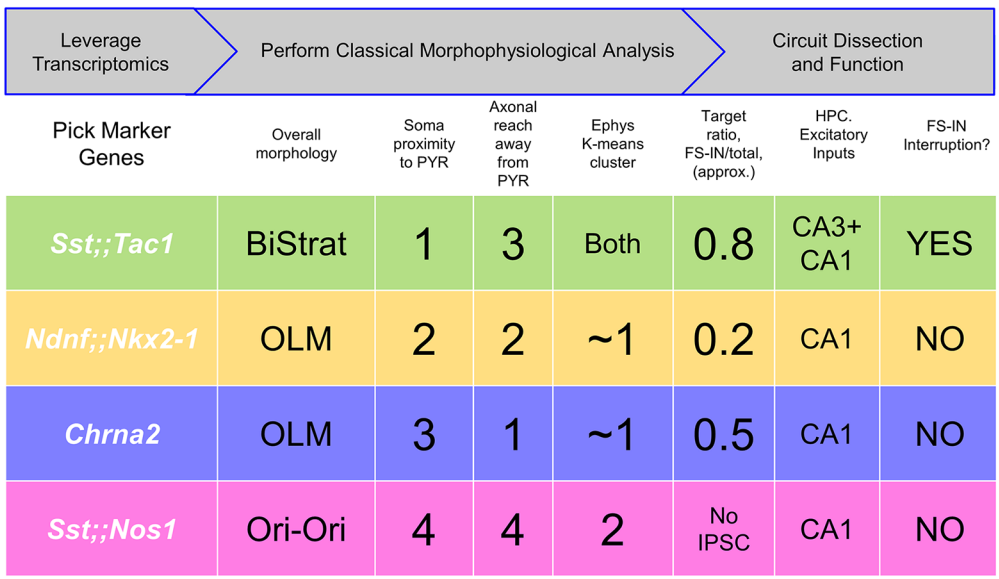

Fig. 6. Approach to subdivide a neuronal family into functionally distinct subclasses based on transcriptomics, morphophysiological analysis, and optogenetic assessment of impact. *Top* rows, Summary of overall workflow (gray arrows) and operational steps. *Bottom* rows, Summary of four subpopulations and some defining characteristics, including morphological ranking with regard to soma proximity to pyramidal layer and axonal extension away from pyramidal layer (Fig. 1); membership in electrophysiological clusters (Fig. 2); optogenetically assessed postsynaptic targeting (Fig. 3); functional impact (Fig. 4); and synaptic recruitment in the hippocampal circuit (Fig. 5).

maintained as double homozygous. *Ndnf;;Nkx2-1* animals were obtained by crossing *Ndnf*-Flp with *Nkx2-1*-Cre [C57BL/6 J-Tg(Nkx2-1-cre)2Sand/J, JAX stock #008661, (70)] animals. *Ndnf*-Flp animals were generated in collaboration with the New York University Langone Medical Center Rodent Genetic Engineering Laboratory. In brief, a T2A-Flpo-pA cassette was inserted immediately following the last codon in the NDNF open reading frame via homologous recombination in ES cells (B4), followed by clone selection and germline transmission from chimeric founders to establish the colony. *Sst;;Nos1* animals were obtained by crossing *Sst*-Flp to *Nos1*-CreER [B6;129S-Nos1$^{tm1.1(cre/ERT2)Zjh}$/J, JAX stock #014541, (60)] animals. *Sst;;Nos1* animals were maintained as homozygous for *Sst*-Flp and heterozygous for *Nos1*-CreER; double homozygous animals were not viable in our initial observations. *Chrna2*-Cre (Tg(Chrna2-cre)1Kldr) were generated in Uppsala University (Sweden) (11) and maintained as hemizygous. *Pv*-Cre [B6.129P2-Pvalb$^{tm1(cre)Arbr}$/J, JAX stock #017320] mice were obtained from The Jackson Laboratory. These animals were then bred to the following homozygous reporter lines: Ai9 [B6.Cg-Gt(ROSA)26Sor$^{tm9(CAG-tdTomato)Hze}$/J, JAX stock #007909, (71)], Ai65 [B6;129S-Gt(ROSA)26Sor$^{tm65.1(CAG-tdTomato)Hze}$/J, JAX stock #021875, (72)], Ai32 [B6.Cg-Gt(ROSA)26Sor$^{tm32(CAG-COP4*H134R/EYFP)Hze}$/J, JAX stock #024109, (73)], Ai80 [B6.Cg-Gt(ROSA)26Sor$^{tm80.1(CAG-COP4*L132C/EYFP)Hze}$/J, JAX stock #025109, (59)]. Tamoxifen was administered to *Sst;;Nos1* animals to induce recombination. Tamoxifen (Sigma-Aldrich, T5648) was dissolved in corn oil at 20 mg/mL, in a heated (55 °C) water bath by vortexing every 2 h. Animals were gavaged every other day with three doses of 0.15 mL tamoxifen-containing corn oil. P20–35 animals were used for experiments described below.

Acute Hippocampal Slice Preparation. For acute slice preparation, animals were deeply anesthetized with isoflurane before decapitation. The brain was rapidly extracted into a sucrose-based ice-cold and oxygenated (95% O_2, 5% CO_2) artificial cerebrospinal fluid (sucrose aCSF). Sucrose aCSF contained (in mM) 185 sucrose, 25 $NaHCO_3$, 2.5 KCl, 25 glucose, 1.25 NaH_2PO_4, 10 $MgCl_2$, and 0.5 $CaCl_2$; pH 7.4, 330 mOsm. After hemisecting the brain, both hemispheres were glued on a platina. Acute hippocampal slices were prepared on a VT1000 S or VT1200 S Vibratome (Leica). Acute slices were then transferred to a heated (32 °C) and oxygenated artificial cerebrospinal fluid (normal aCSF) that contained (in mM) 125 NaCl, 25 $NaHCO_3$, 2.5 KCl, 10 glucose, 2 $CaCl_2$, and 2 $MgCl_2$; pH 7.4, 300 mOsm. Slices were incubated at 32 °C for 30 min, following which the water bath was turned off and the slices were left to recover for an additional 30 min before beginning experiments. Slices were then maintained at room temperature for the rest of the day and slices were used for up to 6 h following preparation.

Electrophysiological Recordings. Acute hippocampal slices were transferred to a recording chamber and held under a harp. The recording chamber was continuously perfused (2 mL/min) with oxygenated aCSF at room temperature (20 ± 2 °C, mean ± SD). An upright microscope (BX50WI or BX61WI, Olympus) equipped with a 40X water-immersion objective was used to visualize the hippocampus. Whole-cell patch clamp recordings were performed from visually identified interneurons expressing TdTomato (Figs. 1 and 2) or from putative pyramidal, fast-spiking, and regular-spiking interneurons that were then functionally identified (Figs. 3 and 4). Recording electrodes were obtained from borosilicate glass filaments (TW150-4, World Precision Instruments) pulled on a P-97 Micropipette Puller (Sutter Instruments). Electrodes had resistance of 3 to 6 MΩ. These electrodes were filled with a solution composed of (in mM): 130 K-gluconate, 10 HEPES, 2 $MgCl_2.6H_2O$, 2 Mg_2ATP, 0.3 NaGTP, 7 Na_2-Phosphocreatine, 0.6 EGTA, 5 KCl; pH 7.2 and 295 mOsm. For voltage-clamp recordings presented in Fig. 3*C* (triangles) and *SI Appendix*, Fig. S10, the internal solution contained (in mM): 130 Cs-methanesulfonate, 10 HEPES, 2 $MgCl_2.6H_2O$, 4 Mg_2ATP, 0.3 NaGTP, 7 Phosphocreatine di(tris), 0.6 EGTA, and 5 KCl; pH 7.3 and 290 mOsm. The liquid junction potential was not corrected. The electrophysiological signal was amplified with an Axopatch 200B or a MultiClamp 700B and digitized at 10 kHz with a Digidata 1322A (Axon Instruments). The data were recorded on personal computers equipped with Clampex 8.2 and 9.2 programs. The data were saved on a personal computer. Cells with resting Vm more depolarized than −45 mV or with access resistance >30 MΩ were not included in the analysis. Optogenetic stimulation was delivered through an optical fiber positioned in *stratum oriens* with a micromanipulator. Blue light (470 nm) was generated by a light-emitting diode (LED) and precisely delivered by a TTL signal originating from the digitizer and sent to the LED controller (WT&T Inc.).

Biocytin Revelation and Confocal Microscopy. Following whole-cell recordings, acute hippocampal slices were fixed with freshly prepared PBS solution containing 4% PFA and left in the fridge overnight. The fixed acute hippocampal slices were processed for biocytin revelation. Briefly, slices were rinsed with PBS (4 × 5 min), treated with H_2O_2 (0.3%, 30 min), permeabilized with Triton (1%, 1 h), and exposed to a streptavidin-conjugated Alexa-633 (1:200, overnight). Slices were rinsed with PBS (4 × 5 min) and mounted on microscope slides with ProLong Gold (ThermoFisher Scientific). Slices were kept in the fridge for at least 2 wk before confocal imaging. Microscope slides with recovered neurons were imaged under an upright confocal microscope (Axo Imager.Z2, Zeiss). The soma location was identified under a low-magnification objective (5×). A 40× oil-immersion objective was used for image acquisition. Z-stacks were acquired through the full Z-axis, in a concentric manner from the soma. We followed axonal and dendritic branches to their termination zones.

Analysis of Single-Cell Transcriptomic Dataset. We used the single-cell transcriptomic dataset from Harris et al. (3), accessed at https://figshare.com/articles/dataset/Transcriptomic_analysis_of_CA1_inhibitory_interneurons/6198656. Genes with no expression were eliminated, and we first focused on the genes determined to define interneurons subclasses. For each gene pair, the product of the expression level was computed. A filter of 50 to 400 neurons was set for putative cluster identification. The neurons with an expression product >1 for individual gene pairs were then identified. The interquartile range and standard distance were measured from the X–Y coordinates of these neurons on the figure 2 presented in Harris et al. (3). We then ranked these putative subclusters based on the weighted average between the standard distance and the interquartile range to identify the top 50 gene pairs for each gene defining interneuron subclasses. While multiple genes and pairs of genes could in theory allow us to target the same clusters, we preferentially used those for which transgenic animals were already available. Despite not fitting the above criteria completely, the *Sst;;Nos1* animals were generated with prior knowledge that these animals identify a very scarce population of INs in the cortex and likely with a low density in the hippocampus (29), hinting that this intersection might target a relatively sparse and well defined population of interneurons.

Neurolucida Reconstructions and Anatomical Analysis. Confocal images were used to reconstruct the morphology of biocytin-filled neurons with the Neurolucida 360 software. Following complete tracing of the neurites, 10-μm-thick contours were drawn over the entirety of the neuron. The border between *strata pyramidale* and *radiatum* was used as a landmark to measure perpendicular distances. Axonal density was then quantified in Neurolucida Explorer by summing the total axon length in each contour. These lengths were averaged across all cells for *Sst*-INs, *Sst;;Tac1*-INs, *Ndnf;;Nkx2-1*-INs, *Chrna2*-INs, and *Sst;;Nos1*-INs. To calculate the cumulative distribution of axon length for each cell type, the total length of axon in each contour was normalized to the summed axon length for that cell. These normalized length distributions were then averaged across cells for individual genotypes. For axon distribution analysis (Fig. 1*H* and *SI Appendix*, Fig. S8 and Table S1), only cells with total axonal length >450 μm were included, and only axonal arborization in CA1 was considered. For dendritic tree analysis (*SI Appendix*, Fig. S8 and Table S1), only cells with total dendritic length >300 μm were included. Anatomical classification (OLM, bistratified and oriens-oriens) was based exclusively on axonal distribution and only cells with total axonal length >450 μm were included. Considering that the total axonal arborization recovered per cell was variable, and that longer axons are more likely to be cut in slices, we established the following set of logical criteria to classify cells: 1) oriens-oriens cells: >50% of axon in st. oriens, <20% in st. radiatum and <20% in st. lacunosum moleculare; 2) bistratified cells: >60% of axon in st. oriens and radiatum, >20% of axon in st. radiatum, <30% of axon in st. lacunosum moleculare; 3) OLM cells: >30% of axon in st. lacunosum moleculare and >40% of axon in st. lacunosum moleculare and oriens. Using these criteria, no cell was found in two categories and only two cells could not be classified. Sankey diagrams in Fig. 1*I* were generated using https://SankeyMATIC.com.

Data Analysis, Statistical Tests, and K-means Analysis. Electrophysiological data were analyzed in Clampfit 10.3 (Molecular Devices) and results were compiled in Microsoft Excel. Kolmogorov–Smirnov tests on anatomical and electrophysiological parameters were performed in GraphPad Prism for macOS (Version 9.5.1). *P*-values reported in *SI Appendix*, Tables S1 and S2 were corrected for multiple comparison using the Holm–Bonferroni method. Normality of data distribution was evaluated with a Shapiro–Wilk test. For normally distributed data, Student's *t* test was used to evaluate statistical significance. For non-normally distributed data, a Mann–Whitney *U* test was used. The EPSP latency was measured from the peak of the stimulation artifact to the inflection point of the EPSP. The action potential latency was measured from the peak of the stimulation artifact to the peak of the action potential. Input resistance was measured from a +10 mV step depolarization in voltage-clamp, and the membrane time constant was measured in current-clamp by fitting an exponential to the recovering phase of a step that hyperpolarized Vm between −10 and −5 mV. Principal component analysis (PCA) was carried out for 81 neurons using the following eight electrophysiological properties: action potential amplitude, threshold, maximum rate of decay, maximum rate of rise, full width at half maximum, afterhyperpolarization maximal amplitude, sag amplitude, and rebound depolarization. Scikit's sklearn.decomposition. PCA function was used to calculate the transformation of this dataset. The absolute values in the eigenvectors corresponding to each property were used to determine the importance of the features within each principal component (*SI Appendix*, Table S3). The first four principal components accounted for more than 90% of the variance of the dataset and so were used for subsequent K-means clustering analysis. For K-means clustering, scikit's sklearn.cluster.kmeans function was first used to determine the optimal value of k via the elbow method. Scipy's scipy.cluster.vq.kmeans2 function was used to distribute the dataset into two clusters using the K-means algorithm. The algorithm is optimized to form clusters with minimal Euclidean distance between each data point and its assigned centroid, which represents the arithmetic mean of the data points in a particular cluster.

Data, Materials, and Software Availability. All original code used in this study is available at https://doi.org/10.5281/zenodo.10815380 (74). Digital reconstructions of neurons are publicly available on NeuroMorpho (https://neuromorpho.org). The raw electrophysiological and microscopy data reported in this manuscript are available upon reasonable request to S.C. or R.W.T.

ACKNOWLEDGMENTS. We thank Dr. Bernardo Rudy for providing the *Ndnf*-Flp mouse, Raquel Moya for help with PCA and K-means analyses, and Ethan Jurman for help with neuronal tracings. S.C. was supported by a senior biomedical postdoctoral fellowship from the Charles H. Revson Foundation, a postdoctoral fellowship from the Fonds de Recherche en Santé Québec, a K99/R00 Pathway to Independence Award from NIMH (1K99MH126157-01), and the Andrew Ellis and Emily Segal Investigator Grant from the Brain and Behavior Research Foundation. R.M. was supported by the NINDS (P01NS074972). K.K. received grants from Swedish Research Council (2022-01245), Swedish Brain Foundation (FO2022-0018) and Olle Engkvist Foundation (462193024). R.W.T. received grants from the NINDS (1U19NS107616-02), NIDA (R01 DA040484-04), and NIMH (R01 MH071739-15), and from the Fresco and Burnett Family Foundations and the Vulnerable Brain Project. We thank the New York University Langone Medical Center Rodent Genetic Engineering Laboratory (P30CA016087).

Author affiliations: [a]New York University Neuroscience Institute, New York University Grossman School of Medicine, New York University, New York, NY 10016; [b]Department of Neuroscience and Physiology, New York University, New York, NY 10016; [c]Developmental Genetics, Department of Neuroscience, Uppsala University, Uppsala, Uppsala län 752 37, Sweden; and [d]Center for Neural Science, New York University, New York, NY 10003

Author contributions: S.C. and R.W.T. designed research; S.C., G.G., and J.S. performed research; R.M., G.T., and K.K. contributed new reagents/analytic tools; S.C., G.G., E.R.N., J.S., and M.H. analyzed data; and S.C., K.K., and R.W.T. wrote the paper.

Reviewers: L.L.G., Duke University; J.M., Baylor College of Medicine; and S.F.O., Stanford University School of Medicine.

1. T. F. Freund, G. Buzsaki, Interneurons of the hippocampus. *Hippocampus* **6**, 347–470 (1996).
2. K. A. Pelkey *et al.*, Hippocampal GABAergic inhibitory interneurons. *Physiol. Rev.* **97**, 1619–1747 (2017).
3. K. D. Harris *et al.*, Classes and continua of hippocampal CA1 inhibitory neurons revealed by single-cell transcriptomics. *PLoS Biol.* **16**, e2006387 (2018).
4. B. Rudy, G. Fishell, S. Lee, J. Hjerling-Leffler, Three groups of interneurons account for nearly 100% of neocortical GABAergic neurons. *Dev. Neurobiol.* **71**, 45–61 (2011).
5. T. Klausberger, P. Somogyi, Neuronal diversity and temporal dynamics: The unity of hippocampal circuit operations. *Science* **321**, 53–57 (2008).
6. S. Royer *et al.*, Control of timing, rate and bursts of hippocampal place cells by dendritic and somatic inhibition. *Nat. Neurosci.* **15**, 769–775 (2012).
7. F. Pouille, M. Scanziani, Routing of spike series by dynamic circuits in the hippocampus. *Nature* **429**, 717–723 (2004).
8. J. C. Lacaille, A. L. Mueller, D. D. Kunkel, P. A. Schwartzkroin, Local circuit interactions between oriens/alveus interneurons and CA1 pyramidal cells in hippocampal slices: Electrophysiology and morphology. *J. Neurosci.* **7**, 1979–1993 (1987).
9. M. Lovett-Barron *et al.*, Regulation of neuronal input transformations by tunable dendritic inhibition. *Nat. Neurosci.* **15**, S421–S423 (2012).
10. A. D. Milstein *et al.*, Inhibitory gating of input comparison in the CA1 microcircuit. *Neuron* **87**, 1274–1289 (2015).
11. R. N. Leao *et al.*, OLM interneurons differentially modulate CA3 and entorhinal inputs to hippocampal CA1 neurons. *Nat. Neurosci.* **15**, 1524–1530 (2012).
12. S. Siwani *et al.*, OLMalpha2 cells bidirectionally modulate learning. *Neuron* **99**, 404–412.e403 (2018).
13. C. Muller, S. Remy, Dendritic inhibition mediated by O-LM and bistratified interneurons in the hippocampus. *Front. Synaptic. Neurosci.* **6**, 23 (2014).
14. S. A. Booker, I. Vida, Morphological diversity and connectivity of hippocampal interneurons. *Cell Tissue Res.* **373**, 619–641 (2018).
15. L. Katona *et al.*, Sleep and movement differentiates actions of two types of somatostatin-expressing GABAergic interneuron in rat hippocampus. *Neuron* **82**, 872–886 (2014).
16. R. Chittajallu *et al.*, Dual origins of functionally distinct O-LM interneurons revealed by differential 5-HT(3A)R expression. *Nat. Neurosci.* **16**, 1598–1607 (2013).
17. S. Mikulovic, C. E. Restrepo, M. M. Hilscher, K. Kullander, R. N. Leao, Novel markers for OLM interneurons in the hippocampus. *Front. Cell Neurosci.* **9**, 201 (2015).
18. P. Somogyi, T. Klausberger, Defined types of cortical interneurone structure space and spike timing in the hippocampus. *J. Physiol.* **562**, 9–26 (2005).
19. Y. Ma, H. Hu, A. S. Berrebi, P. H. Mathers, A. Agmon, Distinct subtypes of somatostatin-containing neocortical interneurons revealed in transgenic mice. *J. Neurosci.* **26**, 5069–5082 (2006).
20. L. Katona *et al.*, Behavior-dependent activity patterns of GABAergic long-range projecting neurons in the rat hippocampus. *Hippocampus* **27**, 359–377 (2017).
21. S. Chamberland *et al.*, Brief synaptic inhibition persistently interrupts firing of fast-spiking interneurons. *Neuron* **111**, 1264–1281.e5 (2023), 10.1016/j.neuron.2023.01.017.
22. J. Artinian, J. C. Lacaille, Disinhibition in learning and memory circuits: New vistas for somatostatin interneurons and long-term synaptic plasticity. *Brain Res. Bull.* **141**, 20–26 (2018).
23. I. Katona, L. Acsady, T. F. Freund, Postsynaptic targets of somatostatin-immunoreactive interneurons in the rat hippocampus. *Neuroscience* **88**, 37–55 (1999).
24. H. Xu, H. Y. Jeong, R. Tremblay, B. Rudy, Neocortical somatostatin-expressing GABAergic interneurons disinhibit the thalamorecipient layer 4. *Neuron* **77**, 155–167 (2013).
25. Z. Yao *et al.*, A taxonomy of transcriptomic cell types across the isocortex and hippocampal formation. *Cell* **184**, 3222–3241.e3226 (2021).
26. R. Tremblay, S. Lee, B. Rudy, Gabaergic interneurons in the neocortex: From cellular properties to circuits. *Neuron* **91**, 260–292 (2016).
27. B. Tasic *et al.*, Shared and distinct transcriptomic cell types across neocortical areas. *Nature* **563**, 72–78 (2018).
28. L. Tricoire *et al.*, A blueprint for the spatiotemporal origins of mouse hippocampal interneuron diversity. *J. Neurosci.* **31**, 10948–10970 (2011).
29. M. He *et al.*, Strategies and tools for combinatorial targeting of GABAergic neurons in mouse cerebral cortex. *Neuron* **92**, 555 (2016).
30. T. Klausberger *et al.*, Spike timing of dendrite-targeting bistratified cells during hippocampal network oscillations in vivo. *Nat. Neurosci.* **7**, 41–47 (2004).
31. G. Maccaferri, C. J. McBain, The hyperpolarization-activated current (Ih) and its contribution to pacemaker activity in rat CA1 hippocampal stratum oriens-alveus interneurones. *J. Physiol.* **497**, 119–130 (1996).
32. J. J. Tukker, P. Fuentealba, K. Hartwich, P. Somogyi, T. Klausberger, Cell type-specific tuning of hippocampal interneuron firing during gamma oscillations in vivo. *J. Neurosci.* **27**, 8184–8189 (2007).
33. C. K. Pfeffer, M. Xue, M. He, Z. J. Huang, M. Scanziani, Inhibition of inhibition in visual cortex: The logic of connections between molecularly distinct interneurons. *Nat. Neurosci.* **16**, 1068–1076 (2013).
34. A. Losonczy, L. Zhang, R. Shigemoto, P. Somogyi, Z. Nusser, Cell type dependence and variability in the short-term plasticity of EPSCs in identified mouse hippocampal interneurones. *J. Physiol.* **542**, 193–210 (2002).
35. E. L. Sylwestrak, A. Ghosh, Elfn1 regulates target-specific release probability at CA1-interneuron synapses. *Science* **338**, 536–540 (2012).
36. A. B. Ali, A. M. Thomson, Facilitating pyramid to horizontal oriens-alveus interneurone inputs: Dual intracellular recordings in slices of rat hippocampus. *J. Physiol.* **507**, 185–199 (1998).
37. A. B. Ali, J. Deuchars, H. Pawelzik, A. M. Thomson, CA1 pyramidal to basket and bistratified cell EPSPs: Dual intracellular recordings in rat hippocampal slices. *J. Physiol.* **507**, 201–217 (1998).
38. P. Parra, A. I. Gulyas, R. Miles, How many subtypes of inhibitory cells in the hippocampus? *Neuron* **20**, 983–993 (1998).
39. E. H. Buhl, K. Halasy, P. Somogyi, Diverse sources of hippocampal unitary inhibitory postsynaptic potentials and the number of synaptic release sites. *Nature* **368**, 823–828 (1994).
40. E. H. Buhl, T. Szilagyi, K. Halasy, P. Somogyi, Physiological properties of anatomically identified basket and bistratified cells in the CA1 area of the rat hippocampus in vitro. *Hippocampus* **6**, 294–305 (1996).
41. G. Maccaferri, J. D. Roberts, P. Szucs, C. A. Cottingham, P. Somogyi, Cell surface domain specific postsynaptic currents evoked by identified GABAergic neurones in rat hippocampus in vitro. *J. Physiol.* **524**, 91–116 (2000).
42. H. Pawelzik, A. P. Bannister, J. Deuchars, M. Ilia, A. M. Thomson, Modulation of bistratified cell IPSPs and basket cell IPSPs by pentobarbitone sodium, diazepam and Zn2+: Dual recordings in slices of adult rat hippocampus. *Eur. J. Neurosci.* **11**, 3552–3564 (1999).

43. G. F. Turi *et al.*, Vasoactive intestinal polypeptide-expressing interneurons in the hippocampus support goal-oriented spatial learning. *Neuron* **101**, 1150–1165.e1158 (2019).
44. S. Chamberland, C. Salesse, D. Topolnik, L. Topolnik, Synapse-specific inhibitory control of hippocampal feedback inhibitory circuit. *Front. Cell Neurosci.* **4**, 130 (2010).
45. L. Acsady, T. J. Gorcs, T. F. Freund, Different populations of vasoactive intestinal polypeptide-immunoreactive interneurons are specialized to control pyramidal cells or interneurons in the hippocampus. *Neuroscience* **73**, 317–334 (1996).
46. L. Tyan *et al.*, Dendritic inhibition provided by interneuron-specific cells controls the firing rate and timing of the hippocampal feedback inhibitory circuitry. *J. Neurosci.* **34**, 4534–4547 (2014).
47. W. Munoz, R. Tremblay, D. Levenstein, B. Rudy, Layer-specific modulation of neocortical dendritic inhibition during active wakefulness. *Science* **355**, 954–959 (2017).
48. N. Holderith, M. Aldahabi, Z. Nusser, Selective enrichment of Munc13-2 in presynaptic active zones of hippocampal pyramidal cells that innervate mGluR1alpha expressing interneurons. *Front. Synaptic. Neurosci.* **13**, 773209 (2021).
49. J. Beninger, J. Rossbroich, K. Tóth, R. Naud, Functional subtypes of synaptic dynamics in mouse and human. *Cell Rep.* **43**, 113785 (2024) https://doi.org/10.1101/2023.05.23.541971.
50. J. Winterer *et al.*, Single-cell RNA-Seq characterization of anatomically identified OLM interneurons in different transgenic mouse lines. *Eur. J. Neurosci.* **50**, 3750–3771 (2019).
51. N. W. Gouwens *et al.*, Integrated morphoelectric and transcriptomic classification of cortical GABAergic cells. *Cell* **183**, 935–953.e919 (2020).
52. C. R. Cadwell *et al.*, Electrophysiological, transcriptomic and morphologic profiling of single neurons using Patch-seq. *Nat. Biotechnol.* **34**, 199–203 (2016).
53. F. Scala *et al.*, Phenotypic variation of transcriptomic cell types in mouse motor cortex. *Nature* **598**, 144–150 (2021).
54. A. Paul *et al.*, Transcriptional architecture of synaptic communication delineates GABAergic neuron identity. *Cell* **171**, 522–539.e520 (2017).
55. C. Foldy *et al.*, Single-cell RNAseq reveals cell adhesion molecule profiles in electrophysiologically defined neurons. *Proc. Natl. Acad. Sci. U.S.A.* **113**, E5222–E5231 (2016).
56. A. Kepecs, G. Fishell, Interneuron cell types are fit to function. *Nature* **505**, 318–326 (2014).
57. E. S. Boyden, F. Zhang, E. Bamberg, G. Nagel, K. Deisseroth, Millisecond-timescale, genetically targeted optical control of neural activity. *Nat. Neurosci.* **8**, 1263–1268 (2005).
58. Z. J. Huang, W. Yu, C. Lovett, S. Tonegawa, Cre/loxP recombination-activated neuronal markers in mouse neocortex and hippocampus. *Genesis* **32**, 209–217 (2002).
59. T. L. Daigle *et al.*, A suite of transgenic driver and reporter mouse lines with enhanced brain-cell-type targeting and functionality. *Cell* **174**, 465–480.e422 (2018).
60. H. Taniguchi *et al.*, A resource of Cre driver lines for genetic targeting of GABAergic neurons in cerebral cortex. *Neuron* **71**, 995–1013 (2011).
61. L. E. Fenno *et al.*, Comprehensive dual- and triple-feature intersectional single-vector delivery of diverse functional payloads to cells of behaving mammals. *Neuron* **107**, 836–853.e811 (2020).
62. V. S. Sohal, F. Zhang, O. Yizhar, K. Deisseroth, Parvalbumin neurons and gamma rhythms enhance cortical circuit performance. *Nature* **459**, 698–702 (2009).
63. J. Dimidschstein *et al.*, A viral strategy for targeting and manipulating interneurons across vertebrate species. *Nat. Neurosci.* **19**, 1743–1749 (2016).
64. G. Pouchelon *et al.*, A versatile viral toolkit for functional discovery in the nervous system. *Cell Rep. Methods* **2**, 100225 (2022).
65. D. Vormstein-Schneider *et al.*, Viral manipulation of functionally distinct interneurons in mice, non-human primates and humans. *Nat. Neurosci.* **23**, 1629–1636 (2020).
66. Y. Qian *et al.*, Programmable RNA sensing for cell monitoring and manipulation. *Nature* **610**, 713–721 (2022).
67. S. J. Wu *et al.*, Cortical somatostatin interneuron subtypes form cell-type–specific circuits. *Neuron* **111**, 2675–2692.e2679 (2023).
68. R. E. Hostetler, H. Hu, A. Agmon, Genetically defined subtypes of layer 5 somatostatin-containing cortical interneurons. *eNeuro*. **10**, (2023) https://doi.org/10.1101/2023.02.02.526850.
69. J. A. Harris *et al.*, Anatomical characterization of Cre driver mice for neural circuit mapping and manipulation. *Front. Neural Circ.* **8**, 76 (2014).
70. Q. Xu, M. Tam, S. A. Anderson, Fate mapping Nkx2.1-lineage cells in the mouse telencephalon. *J. Comp. Neurol.* **506**, 16–29 (2008).
71. L. Madisen *et al.*, A robust and high-throughput Cre reporting and characterization system for the whole mouse brain. *Nat. Neurosci.* **13**, 133–140 (2010).
72. L. Madisen *et al.*, Transgenic mice for intersectional targeting of neural sensors and effectors with high specificity and performance. *Neuron* **85**, 942–958 (2015).
73. L. Madisen *et al.*, A toolbox of Cre-dependent optogenetic transgenic mice for light-induced activation and silencing. *Nat. Neurosci.* **15**, 793–802 (2012).
74. S. Chamberland, G. Grant *et al.*, Functional specialization of hippocampal somatostatin-expressing interneurons – Code for PCA and k-means clustering. Zenodo. https://doi.org/10.5281/zenodo.10815380. Deposited 13 March 2024.